mathematics

Article

Multiobjective Collaborative Optimization of Argon Bottom Blowing in a Ladle Furnace Using Response Surface Methodology

Zicheng Xin [1], Jiankun Sun [1], Jiangshan Zhang [1,*], Bingchang He [1], Junguo Zhang [2] and Qing Liu [1,*]

[1] State Key Laboratory of Advanced Metallurgy, University of Science and Technology Beijing, Beijing 100083, China; sklxzc@163.com (Z.X.); hblgsjk@163.com (J.S.); becher97@163.com (B.H.)
[2] Tangshan Branch, Hebei Iron and Steel Co., Ltd., Tangshan 063000, China; zhangjgtg@163.com
* Correspondence: qliu@ustb.edu.cn (Q.L.); zjsustb@163.com (J.Z.)

Abstract: In order to consider both the refining efficiency of the ladle furnace (LF) and the quality of molten steel, the water model experiment is carried out. In this study, the single factor analysis, central composite design principle, response surface methodology, visual analysis of response surface, and multiobjective optimization are used to obtain the optimal arrangement scheme of argon blowing of LF, design the experimental scheme, establish the prediction models of mixing time (*MT*) and slag eye area (*SEA*), analyze the comprehensive effects of different factors on *MT* and *SEA*, and obtain the optimal process parameters, respectively. The results show that when the identical porous plug radial position is 0.6R and the separation angle is 135°, the mixing behavior is the best. Moreover, the optimized parameter combination is obtained based on the response surface model to simultaneously meet the requirements of short *MT* and small *SEA* in the LF refining process. Meanwhile, compared with the predicted values, the errors of *MT* and *SEA* for different conditions from the experimental values are 1.3% and 2.1%, 1.3% and 4.2%, 2.5% and 3.4%, respectively, which is beneficial to realizing the modeling of argon bottom blowing in the LF refining process and reducing the interference of human factors.

Keywords: ladle furnace; argon bottom blowing; hydraulic experiment; mixing time; slag eye area; multiobjective collaborative optimization; response surface methodology

MSC: 62J05

check for updates

Citation: Xin, Z.; Sun, J.; Zhang, J.; He, B.; Zhang, J.; Liu, Q. Multiobjective Collaborative Optimization of Argon Bottom Blowing in a Ladle Furnace Using Response Surface Methodology. *Mathematics* **2022**, *10*, 2610. https://doi.org/10.3390/math10152610

Academic Editor: János Sztrik

Received: 24 June 2022
Accepted: 22 July 2022
Published: 26 July 2022

1. Introduction

Ladle furnace (LF) refining has been widely used in steelmaking plants thanks to its multiple advantages [1,2]. As one of the main functions of LF refining, argon bottom blowing of LF has an important influence on the refining efficiency and quality of molten steel. In the LF refining process, unreasonable arrangement of argon bottom blowing and operation processes will lead to low refining efficiency and even cause serious secondary oxidation of molten steel, which affects the quality of molten steel. Therefore, many researchers carried out a lot of studies by physical simulation and numerical simulation to analyze the effects of gas flow rate [3], liquid depth [4], slag thickness [5], porous plug radial position and separation angle [6,7], and tracer addition position [8] on the mixing time (*MT*).

Mandal et al. [9] studied the influences of gas flow rate, liquid depth and ladle radius on *MT*, and obtained the calculation formula of *MT* based on the experimental data. Zhu et al. [10] proposed a mathematical model for mixing time in the ladle considering the number of tuyeres, and the predicted values are in good agreement with the experimental values. Morales et al. [11] studied the influence of slag thickness on the fluid dynamics of argon bottom blowing of LF by physical simulation and numerical simulation and concluded that increasing the slag thickness could increase the *MT* and reduce slag eye area (*SEA*). Herrera-Ortega et al. [8] studied the influence of the additional position of tracer on *MT* through physical and numerical simulation, and the results showed that *MT* changed with the change of the additional position of tracer, which was related to the turbulent viscosity to some extent. Meanwhile, the effects of gas flow rate [12], liquid depth [13], slag thickness [14] and physical properties of slag [15] on *SEA* were studied. Conejo et al. [16] studied the effects of gas flow rate, porous plug radial position and separation angle on the *MT*, *SEA* and wall shear stress, and the results showed that it was beneficial to improve the mixing effect of the ladle when the identical porous plug radial position was 0.7R, the separation angle was 45° and the gas flow rate was equal; compared with the identical porous plug radial position, when the porous plug radial position was different (0.7R/0.5R), the separation angle was 90°, and the gas flow rate was not equal (1:3), it was beneficial to reduce the *SEA* and the shear stress between molten steel and the ladle wall. Subsequently, the existing experimental data of ladle *SEA* were re-evaluated based on dimensional analysis, and the dimensionless calculation formulae of *SEA* for single and double porous plugs were established [17]. Krishnapisharody et al. [18] developed a mechanistic model for eye size, and this model is consistent with the experimental results and those of others in different liquid systems. Peranandhanthan et al. [13] studied the effects of gas flow rate, liquid depth, slag thickness and physical properties of slag on the *SEA* through physical simulation and established the dimensionless calculation formulae for *SEA*. In addition, the results showed that the viscosity and density of slag had a decisive effect on the *SEA*, while the interfacial tension had no effect on the *SEA*. However, the research of Li et al. [15] showed that both the viscosity and the interfacial tension had little effect on the *SEA*.

Reasonable argon bottom blowing of LF can not only reduce *MT* and enhance refining efficiency but also play an important role in improving the quality of molten steel. Many researchers have carried out a large number of studies on the effects of different factors on *MT* and *SEA*, which provides great support for the development of high-efficiency LF refining. However, current studies mostly use the single-factor analysis method to research a single objective (*MT* or *SEA*), and there are, so far, few reports on the optimization of multiple objectives for multiple factors. In the LF refining process, the *MT* can be reduced by increasing the gas flow rate. However, a large gas flow rate will lead to large *SEA* and secondary oxidation of molten steel. Therefore, the effects of different factors on *MT* and *SEA* should be considered comprehensively in the optimization of argon bottom blowing of LF. In terms of multiobjective optimization, Leung et al. [19] proposed a collaborative neurodynamic approach for multiobjective optimization based on the particle swarm optimization algorithm and projection neural network to attain both goals of Pareto optimality and solution diversity. Wang et al. [20] presented an interactive multiobjective optimization-based manufacturing planning system to help the decision maker reach a satisfactory tradeoff between the two objectives without causing a severe computational burden. Nole et al. [21] used an interactive method based on a multiobjective integer linear programming weighted sum scalarization to examine how classroom design affects cognitive processes. Response surface methodology (RSM) is a statistical analysis method of multiobjective collaborative optimization combining experimental design and mathematical modeling. This method has been applied in different fields for its short experimental period and high reliability of the regression equation [22–25]; however, there are few reports on the optimization of argon bottom blowing of LF using RSM.

In this study, according to the similarity principle, the 150 t LF was taken as the research object and the hydraulic experiment was carried out. Firstly, the influences of different identical porous plug radial position and separation angle on *MT* were studied to obtain the optimal arrangement scheme of argon bottom blowing of LF. Then, the effects of gas flow rate, liquid depth and slag thickness on *MT* and *SEA* were studied by single factor analysis. Moreover, the comprehensive effects of gas flow rate, liquid depth and slag thickness on *MT* and *SEA* were studied using RSM. Meanwhile, the prediction models for

MT and *SEA* were established and evaluated. Finally, in order to meet the requirements of short *MT* and small *SEA*, the response surface models were used to obtain the optimal parameters and the model results were verified by a hydraulic experiment.

2. Experimental Principles and Methods

In this study, the hydraulic experiment of *MT* determination and slag eye formation were carried out based on the similarity theory (including geometric similarity, dynamic similarity and steel-slag interface similarity).

2.1. Experimental Principles

2.1.1. Geometric Similarity

The hydraulic experiment takes 150-t ladle as the prototype. The scale factor is 1:4, and the dimensions of the prototype and model are shown in Table 1. In the process of the hydraulic experiment, water was used to simulate molten steel and air was used to simulate argon. The physical properties of various substances are shown in Table 2.

Table 1. Dimensions of prototype and model.

Parameters/mm	Prototype	Model
Top diameter	3000	750
Basal diameter	2651	663
Ladle height	3915	979
Porous plug diameter	120	30

Table 2. Physical properties of various substances [26].

Physical Properties	Water (Normal Temperature)	Steel (1600 °C)	Slag (1600 °C)	Air (Normal Temperature)	Argon (Normal Temperature)
Density (kg/m^3)	1000	7000	3500	1.205	1.784
Dynamic viscosity (Pa·s)	0.001	6.7×10^{-3}	0.13–0.20	-	-
Kinematic viscosity/(10^{-6} m^2·s^{-1})	1.0	0.95	37–57	-	-

2.1.2. Dynamic Similarity

In a gas-liquid two-phase flow system, it is necessary to make the modified Froude number of prototype and model equal to meet the conditions of dynamic similarity [27–30]. The gas flow rate of model can be calculated using the modified Froude number, as shown in Equation (1).

$$Q_{\mathrm{m}} = \left[\frac{\rho_{\mathrm{g,p}}}{\rho_{\mathrm{g,m}}} \frac{\rho_{\mathrm{l,m}}}{\rho_{\mathrm{l,p}}} \left(\frac{d_{\mathrm{m}}}{d_{\mathrm{p}}} \right)^4 \left(\frac{H_{\mathrm{m}}}{H_{\mathrm{p}}} \right) \right]^{1/2} Q_{\mathrm{p}} = 0.01437 Q_{\mathrm{p}} \tag{1}$$

where ρ_{g} and ρ_{l} represent the density of gas and liquid, respectively; H represents the liquid depth; Q represents the gas flow rate; D represents the porous plug diameter; p represents the prototype; m represents the model.

Combined with the actual production and Equation (1), the gas flow rate of the model was obtained, as shown in Table 3.

Table 3. Gas flow rate of prototype and model.

Type	Gas	Gas Flow Rate of Each Porous Plug (NL·min^{-1})				
Prototype	Argon	100	200	300	400	500
Model	Air	1.4	2.9	4.3	5.7	7.2

Note: There are two porous plugs for prototype and model, and these porous plugs have the same gas flow rate.

2.1.3. Steel-Slag Interface Similarity

For the hydraulic experiment containing slag, it is necessary to ensure that the steel-slag interface is similar. Therefore, on the basis of satisfying the geometric similarity and the equality of the modified Froude number, it is necessary to make the Weber number of prototype and model equal.

Based on the equality of Froude number, Equation (2) can be obtained.

$$\frac{u_{\mathrm{water}}^2}{u_{\mathrm{steel}}^2} = \frac{\rho_{\mathrm{Ar}} \cdot \rho_{\mathrm{water}} \cdot H_{\mathrm{m}}}{\rho_{\mathrm{Air}} \cdot \rho_{\mathrm{steel}} \cdot H_{\mathrm{p}}} = \frac{\rho_{\mathrm{Ar}} \cdot \rho_{\mathrm{water}}}{\rho_{\mathrm{Air}} \cdot \rho_{\mathrm{steel}}} \cdot \lambda \tag{2}$$

Based on the equality of Weber number, Equation (3) can be obtained.

$$\rho_{\mathrm{oil}} = \rho_{\mathrm{water}} - \frac{u_{\mathrm{water}}^4 \rho_{\mathrm{water}}^2 \sigma_{\mathrm{steel\text{-}slag}}^2 (\rho_{\mathrm{steel}} - \rho_{\mathrm{slag}})}{u_{\mathrm{steel}}^4 \rho_{\mathrm{steel}}^2 \sigma_{\mathrm{water\text{-}oil}}^2} \tag{3}$$

The density of oil obtained when combining Equations (2) and (3), as expressed in Equation (4).

$$\rho_{\mathrm{oil}} = \rho_{\mathrm{water}} - \frac{\rho_{\mathrm{Ar}}^2 \rho_{\mathrm{water}}^4 \sigma_{\mathrm{steel\text{-}slag}}^2}{\rho_{\mathrm{Air}}^2 \rho_{\mathrm{steel}}^4 \sigma_{\mathrm{water\text{-}oil}}^2} \lambda^2 (\rho_{\mathrm{steel}} - \rho_{\mathrm{slag}}) = 846.473 \approx 846\ \mathrm{kg} \cdot \mathrm{m}^{-3} \tag{4}$$

where u_{water} and u_{steel} represent the characteristic velocities of water and molten steel, respectively; ρ_{water} and ρ_{steel} represent the density of water and molten steel, respectively; $\sigma_{\mathrm{water\text{-}oil}}$ and $\sigma_{\mathrm{steel\text{-}slag}}$ represent interfacial tension of water-oil and steel-slag, respectively. The $\sigma_{\mathrm{water\text{-}oil}}$ [31] and $\sigma_{\mathrm{steel\text{-}slag}}$ [31] are 0.044 $\mathrm{N{\cdot}m^{-1}}$ and 1.22 $\mathrm{N{\cdot}m^{-1}}$, respectively.

The viscosity of slag has a great influence on *SEA*. In order to obtain more accurate experimental results, the kinematic viscosity of oil used to simulate slag should meet Equation (5) [32].

$$\frac{\nu_{\mathrm{steel}}}{\nu_{\mathrm{slag}}} = \frac{\nu_{\mathrm{water}}}{\nu_{\mathrm{oil}}} \tag{5}$$

where v_{steel} represents the kinematic viscosity of molten steel; v_{slag} represents the kinematic viscosity of slag; v_{water} represents the kinematic viscosity of water; v_{oil} represents the kinematic viscosity of oil.

According to Table 2 and Equation (5), the range of kinematic viscosity of oil should be 39–60 $\times 10^{-6}$ $\mathrm{m^2{\cdot}s^{-1}}$. Under normal temperature, the dynamic viscosity, density and kinematic viscosity of abrasion-resistant hydraulic oil are 50 $\times 10^{-3}$ Pa·s, 870 $\mathrm{kg{\cdot}m^{-3}}$ and 57 $\times 10^{-6}$ $\mathrm{m^2{\cdot}s^{-1}}$, respectively, which are basically consistent with the calculated density and kinematic viscosity of experimental oil. Therefore, the abrasion-resistant hydraulic oil was used to simulate slag.

2.2. Experimental Method

The equipment connection diagram of hydraulic experiment is shown in Figure 1. For the experimental determination of *MT*, firstly, the model was filled with the amount of water specified in the experimental scheme, and the gas flow rate was adjusted to the experimental flow rate. Then, a funnel was fixed on the top of the model and the position was consistent with the actual production. After blowing air for 3 min, the flow field in ladle was basically stable. The saturated KCl solution as tracer was added into the model through the funnel. Finally, the electrical conductivity data were collected by conductivity electrode, conductivity meter and DJ800 multi-function monitoring system and the data were transferred to computer to obtain the residence time distribution (RTD) curves. The *MT* was determined according to the changes in the relative electrical conductivities of electrodes are less than 5% of the steady state. The experiment was repeated 3 times for each experimental condition and the average value was taken as the *MT*.

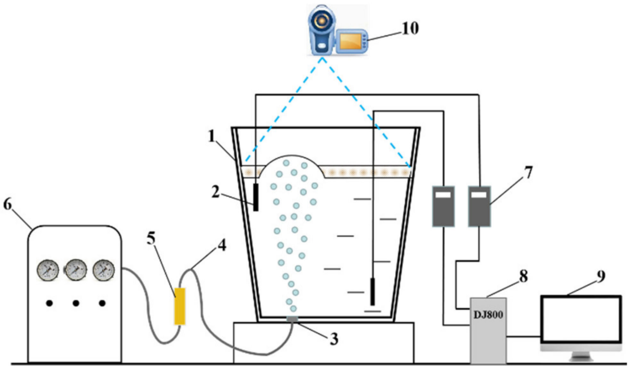

Figure 1. Equipment connection diagram. 1—model; 2—conductivity electrode; 3—porous plug; 4—tube; 5—gas flowmeter; 6—air compressor; 7—conductivity meter; 8—multifunction monitoring system (DJ800); 9—computer; 10—camera.

For hydraulic experiment of slag eye formation, according to the similarity ratio of 1:4, the oil thickness was calculated by combining the actual production. The process of the hydraulic experiment of slag eye formation was the same as that of the hydraulic experiment without slag. The specified amount of water and oil were added to the model and the gas flow rate was set as the experimental flow rate. After the flow field in the ladle was basically stable, the *MT* and *SEA* were measured under different gas flow rates, different liquid depths and different slag thicknesses. For the measurement of *SEA*, firstly, the slag surface was photographed vertically by a camera, as shown in Figure 2a. Secondly, the pixels of the slag eye and the slag surface were calculated using the image processing software (Photoshop), as shown in Figure 2b,c. Then, the percentage of slag eye on slag surface was calculated according to the statistics results of pixel. Finally, the *SEA* was calculated according to the slag surface area.

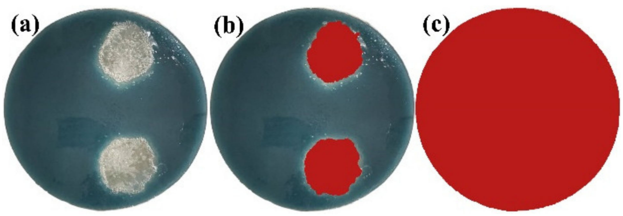

Figure 2. Diagram of slag surface of ladle (Top view). (**a**) Initial diagram; (**b**) pixel statistics of slag eye; (**c**) pixel statistics of slag surface.

3. Experimental Schemes

The single factor analysis was used to design the experimental scheme to obtain the optimal arrangement scheme of argon blowing for LF. Subsequently, based on the optimal arrangement scheme, the experimental scheme was designed to analyze the effects of different factors on *MT* and *SEA*. Moreover, based on the central composite design (CCD) principle, an experimental scheme was designed to establish the prediction models of *MT* and *SEA* and analyze the comprehensive effects of different factors on *MT* and *SEA*.

3.1. Single Factor Analysis Experiment Scheme of Argon Bottom Blowing of LF

The optimal arrangement of argon bottom blowing of LF was evaluated by *MT*. The porous plug radial positions were 0.43R, 0.6R and 0.7R, and the separation angles were 90°, 135° and 180°. The porous plug radial position and separation angle of the prototype were 0.43R and 90°, respectively. The experimental scheme of *MT* measurement is shown in Table 4. Subsequently, based on the optimal arrangement scheme of argon bottom blowing of LF, the effects of gas flow rate, liquid depth and slag thickness on *MT* and *SEA* were analyzed and the experimental scheme is shown in Table 5.

Table 4. Experiment scheme of optimal arrangement of porous plugs.

Number	1	2	3	4	5	6	7	8	9
Separation angle	90°	90°	90°	135°	135°	135°	180°	180°	180°
Porous plug radial location	0.43R	0.6R	0.7R	0.43R	0.6R	0.7R	0.43R	0.6R	0.7R

Table 5. Experiment scheme of single factor analysis.

Number	**1**	**2**	**3**	**4**	**5**
Gas flow rate/(NL·min^{-1})	1.4	2.9	4.3	5.7	7.2
Liquid depth 760.5 mm; Slag thickness 32.5 mm					
Number	**6**	**7**	**8**	**9**	**10**
Liquid depth/mm	653	707	760.5	814	866
Gas flow rate 4.3 NL·min^{-1}; Slag thickness 32.5 mm					
Number	**11**	**12**	**13**	**14**	**15**
Slag thickness/mm	20	26.3	32.5	38.8	45
Gas flow rate 4.3 NL·min^{-1}; Liquid depth 760.5 mm					

3.2. Experimental Scheme and Results of Argon Bottom Blowing of LF Based on RSM

The CCD of the response surface method can be used to analyze the effects of single-factor and multi-factor interactions on the research object [33,34]. Based on the single factor analysis and the CCD principle, an experimental scheme with 3 factors and 5 levels was designed using Minitab software to analyze the effects of gas flow rate, liquid depth and slag thickness on the *MT* and *SEA*. The experimental factors and levels are shown in Table 6. The levels of three factors were set based on the actual production and the similarity principle. In the LF refining process, the range of gas flow rate of a single porous plug was 100–500 NL·min^{-1}. The range of liquid depth was 2611–3463 mm according to the minimum and maximum treatment capacity of molten steel. The value of slag thickness ranged from 80 to 180 mm. According to a similar principle, the ranges of the gas flow rate, liquid depth and slag thickness were 1.4–7.2 NL·min^{-1}, 653–866 mm and 20–45 mm, respectively, in the hydraulic experiment. The experimental scheme is shown in Table 7. It includes 20 experiments and all combinations of the three factors.

Table 6. Experimental factors and levels of CCD experimental design.

Parameters	**Coding**	**Level**				
		−1.68179	**−1**	**0**	**1**	**1.68179**
Gas flow rate/(NL·min^{-1})	A	1.9	2.9	4.3	5.7	6.7
Liquid depth/mm	B	670.5	707	760.5	814	850.5
Slag depth/mm	C	21.6	26	32.5	39	43.4

Table 7. Experimental design and results.

Number	Gas Flow Rate/(NL·min^{-1})	Liquid Depth/mm	Slag Depth/mm	*MT*/s	*SEA*/mm^2
1	2.9	707	26	76	54,767
2	5.7	707	26	65	95,459
3	2.9	814	26	79	56,154
4	5.7	814	26	68	110,356
5	2.9	707	39	83	36,926
6	5.7	707	39	74	66,479
7	2.9	814	39	85	36,724
8	5.7	814	39	79	77,598
9	1.9	760.5	32.5	92	25,141
10	6.7	760.5	32.5	74	96,792
11	4.3	670.5	32.5	69	58,130
12	4.3	850.5	32.5	80	91,154
13	4.3	760.5	21.6	66	96,683
14	4.3	760.5	43.4	79	51,141
15	4.3	760.5	32.5	73	72,446
16	4.3	760.5	32.5	72	73,248
17	4.3	760.5	32.5	75	75,002
18	4.3	760.5	32.5	73	72,529
19	4.3	760.5	32.5	71	75,149
20	4.3	760.5	32.5	69	63,140

4. Results and Discussion

Firstly, the optimal arrangement scheme of argon bottom blowing of LF was obtained by comparing the *MT* under different radial positions and the separation angle of porous plugs. Then, based on the optimal arrangement scheme, the effects of different factors on *MT* and *SEA* were analyzed. Moreover, the prediction models of *MT* and *SEA* were established based on the RSM, and the comprehensive effects of different factors on *MT* and *SEA* were analyzed based on the visual analysis of the response surface. Finally, on the basis of multiobjective optimization, the optimal process parameters of argon blowing for LF were determined and verified by hydraulic experiment.

4.1. Experimental Results of Single Factor Analysis

4.1.1. Effect of Porous Plug Radial Position on MT

Figure 3 shows the effects of gas flow rate, separation angle and radial position of porous plugs on *MT*. In Figure 3a, when the separation angle is 90° and the porous plug radial positions are 0.43R and 0.7R, respectively, the *MT* first decreases and then increases slightly with the increase in gas flow rate. For instance, under the conditions of a porous plug radial position of 0.43R and a separation angle of 90°, when the gas flow rate increases from 1.4 NL·min^{-1} to 5.7 NL·min^{-1}, the *MT* decreases from 102 s to 64 s and the *MT* decreases by 38 s; when the gas flow rate increases continuously to 7.2 NL·min^{-1}, the *MT* increases from 64 s to 67 s and the *MT* increases by 3 s. At a fixed porous plug radial position of 0.6R, the *MT* decreases with increasing the gas flow rate. When the range of the gas flow rate is 2.9–5.7 NL·min^{-1}, the order of the *MT* of different porous plug radial positions, from long to short, is as follows: 0.43R, 0.6R, 0.7R.

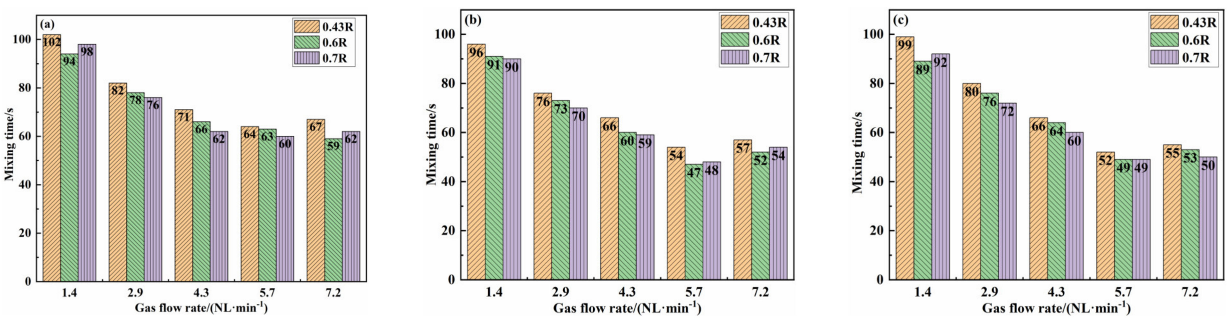

Figure 3. Effect of gas flow rate on *MT* at various radial angle: (**a**) 90°; (**b**) 135°; (**c**) 180°.

In Figure 3b, at a fixed separation angle of 135°, the *MT* first decreases and then increases with the increase in gas flow rate in different porous plug radial positions, and the *MT* reaches its minimum when the gas flow rate is 5.7 NL·min^{-1}. When the range of the gas flow rate is 1.4–4.3 NL·min^{-1}, the order of the *MT* of different porous plug radial positions, from long to short, is as follows: 0.43R, 0.6R, 0.7R; when the gas flow rate is further increased to 5.7 NL·min^{-1}, the order of the *MT* of different porous plug radial positions, from long to short, is as follows: 0.43R, 0.7R, 0.6R.

In Figure 3c, at a fixed separation angle of 180°, the *MT* first decreases and then increases with the increase in gas flow rate in different porous plug radial positions. The analysis reason is that the main function of the bubble is to promote the flow of molten steel and then form a circulating flow. The gas flow rate increases, and the stirring energy increases, which reduces the *MT*. However, when the gas flow rate is increased to exceed some critical value, part of the gas directly spills out from the liquid surface and part of the energy is applied to roll the surface of the liquid, which causes a loss of stirring energy. Additionally, the *MT* is not shortened significantly and even results in a time extension [31]. When the range of the gas flow rate is 2.9–7.2 NL·min^{-1}, the order of the *MT* of different porous plug radial positions, from long to short, is as follows: 0.43R, 0.6R, 0.7R. To sum up, the *MT* decreases with the increase in porous plug radial position. The analysis reason is that with the increase in porous plug radial position, the collision of two rising gas columns is reduced, which leads to the decrease in *MT* [31]. However, when the porous plug radial position is 0.7R, the large gas flow rate leads to serious erosion of the lining of the ladle, which not only reduces the service life of the ladle lining but also increases the *MT*. Therefore, the porous plug radial position of 0.6R is taken as the optimal scheme.

4.1.2. Effect of Porous Plug Separation Angle on MT

Figure 4 shows the effects of gas flow rate, separation angle and radial position of the porous plug on the *MT*. In Figure 4a, at a fixed porous plug radial position of 0.43R, the *MT* first decreases and then increases with the increase in gas flow rate at different separation angles, and the *MT* reaches its minimum when the gas flow rate is 5.7 NL·min^{-1}. When the range of gas flow rate is 1.4–4.3 NL·min^{-1}, the bottom blowing arrangement with a separation angle of 135° has the shortest *MT*. However, the range of gas flow rate is 5.7–7.2 NL·min^{-1}. The bottom-blowing arrangement with a separation angle of 180° has the shortest *MT*. In Figure 4b, at a fixed porous plug radial position of 0.6R, when the separation angle is 90°, the *MT* decreases with the increase in gas flow rate; when the separation angles are 135° and 180°, respectively, the *MT* first decreases and then increases with the increase in gas flow rate. When the separation angle is 135° and the gas flow rate is 5.7 NL·min^{-1}, the shortest *MT* is 47 s. In Figure 4c, at a fixed porous plug radial position of 0.7R, the *MT* first decreases and then increases with the increase in gas flow rate at different separation angles. When the separation angle is 135° and the gas flow rate is 5.7 NL·min^{-1}, the shortest *MT* is 48 s. To sum up, the separation angle of 135° is taken as the optimal scheme.

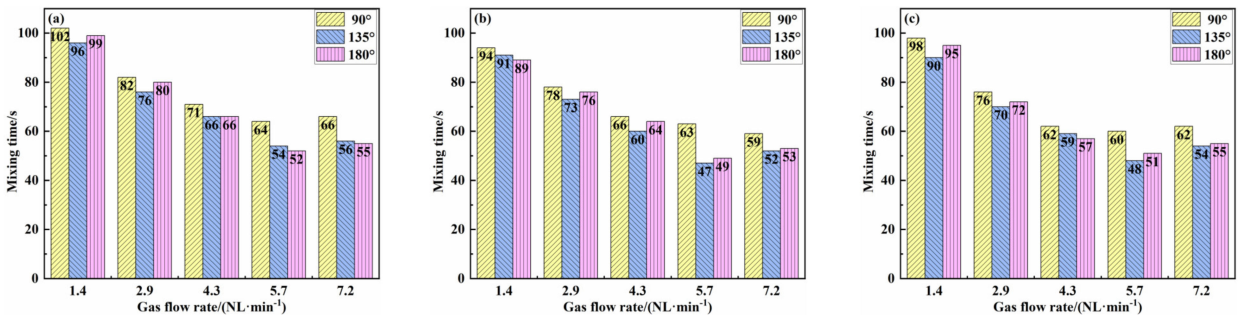

Figure 4. Effect of gas flow rate on *MT* at various radial location: (**a**) 0.43R; (**b**) 0.6R; (**c**) 0.7R.

4.1.3. Effects of Different Factors on *MT* and *SEA*

To improve the mixing efficiency of LF refining, a larger gas flow rate is needed. However, the *SEA* increases with the increase in gas flow rate, which leads to a large amount of molten steel contacting the air and causing serious secondary oxidation of molten steel. Therefore, the research on *SEA* should not be ignored. The effects of different factors on *MT* and *SEA* are shown in Figure 5. In Figure 5a, at a fixed liquid depth of 760.5 mm and a slag thickness of 32.5 mm, the *MT* first decreases and then increases with the increase in gas flow rate and the *MT* reaches its minimum when the gas flow rate is 5.7 NL·min^{-1}. Compared with the condition without slag, the *MT* increases. The analysis reason is that when the bubble rises to the top of the liquid, part of the stirring energy used to break up the slag layer is consumed, which leads to the weakening of the stirring energy of molten steel and an increase in *MT* [3]. The *SEA* increases linearly with the increase in gas flow rate, and the effect of gas flow rate on *SEA* is shown in Figure 6a–e.

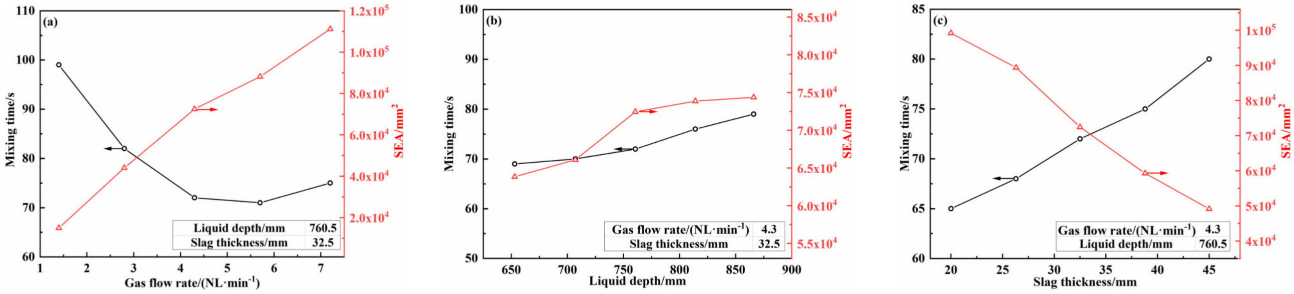

Figure 5. Effect of various factors on *MT* and *SEA* at: (**a**) gas flow rate; (**b**) liquid depth; (**c**) slag thickness.

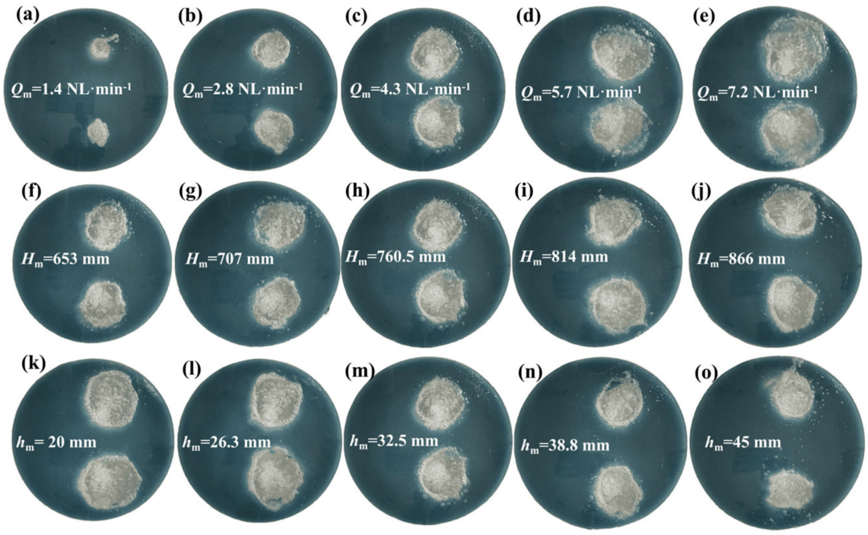

Figure 6. Effect of various factors on *SEA* at: (**a**–**e**) gas flow rate; (**f**–**j**) liquid depth; (**k**–**o**) slag thickness (Top view).

In Figure 5b, at a fixed gas flow rate of 4.3 NL·min^{-1} and a slag thickness of 32.5 mm, the *MT* increases with the increase in liquid depth. The analysis reason is that when the gas flow rate is constant, the mass of molten steel increases with the increase in the depth of molten steel, which leads to a decrease in the stirring energy per unit mass of molten steel and an increase in *MT* [4]. The *SEA* increases with the increase in liquid depth. The analysis reason is that, combined with the plume model [35], when the gas flow rate is high enough to form a slag eye, the length of the horizontal flow direction in the exposed area of the oil layer increases with the increase in liquid depth. Namely, the *SEA* increases. Additionally, the effect of liquid depth on *SEA* is shown in Figure 6f–j.

In Figure 5c, at a fixed gas flow rate of 4.3 NL·min^{-1} and liquid depth of 760.5 mm, the *MT* increases linearly with the increase in slag thickness and the *SEA* decreases linearly with the increase in slag thickness. With the increase in slag thickness, more energy is needed to blow open the slag layer. Therefore, with the increase in slag thickness, the *SEA* decreases at the same gas flow rate [13]. The effect of slag thickness on *SEA* is shown in Figure 6k–o. Moreover, the ladle is tapered, so the liquid surface area at the top varies with the liquid depth and the slag thickness.

4.2. Experimental Results of Argon Bottom Blowing Based on RSM

4.2.1. Establishment of Prediction Models

To obtain the optimal prediction models of *MT* and *SEA*, the linear model, interactive model and complete quadratic model were established by using the experimental data in Table 7. The model summary is listed in Table 8.

Table 8. Model summary.

Source	***MT*/s**			***SEA*/mm^2**		
	Standard Deviation	**R^2**	**Adjusted R^2**	**Standard Deviation**	**R^2**	**Adjusted R^2**
Linear model	3.87	0.7229	0.6709	6741.42	0.9232	0.9088
Interaction model	4.22	0.7314	0.6075	6631.20	0.9396	0.9118
Complete quadratic model	1.87	0.9595	0.9230	5189.62	0.9716	0.9460

In Table 8, for the prediction model of *MT*, it can be seen that the complete quadratic model has the best performance by comparing the standard deviation (*SD*), the goodness of fit (R^2) and adjusted goodness of fit (adjusted R^2) of the linear model, interactive model and complete quadratic model. Additionally, the *SD*, R^2 and adjusted R^2 of the complete quadratic model are 1.87 s, 0.9595 and 0.9230, respectively. This result indicates that the experimental design is reliable and the model fitting is good and acceptable. Therefore, the complete quadratic model is selected to establish the prediction model of *MT*, as shown in Equation (6). Similarly, for the prediction model of *SEA*, the complete quadratic model has the best performance and the *SD*, R^2 and adjusted R^2 of the complete quadratic model are 5189.62 mm^2, 0.9716 and 0.9460, respectively. The fitting formula is shown in Equation (7).

For the prediction model of *MT* is as follows:

$$\begin{aligned} MT &= 238 - 26.5A - 0.337B + 0.01C + 1.866A^2 + 0.000228B^2 \\ &\quad -0.0013C^2 + 0.00501AB + 0.0962AC + 0.00036BC \end{aligned} \tag{6}$$

For the prediction model of *SEA* is as follows:

$$\begin{aligned} SEA &= 57{,}319 + 14{,}039A - 188B + 794C - 2289A^2 + 0.122B^2 \\ &\quad +2.2C^2 + 41.4AB - 336AC - 1.93BC \end{aligned} \tag{7}$$

where *A* is the gas flow rate; *B* is the liquid depth; *C* is the slag thickness.

4.2.2. Analysis of Variance and Model Evaluation

In order to evaluate the credibility of models, analysis of variance (ANOVA) was conducted on the complete quadratic models, as shown in Table 9. The *F*-value is the ratio of mean squares between groups to mean squares within the group. The *p*-value is the probability that the *F*-statistic can take a value larger than the computed test-statistic value. When the *p*-value is less than 0.01, the item of the model is highly significant; when the *p*-value is less than 0.05, the item of the model is significant; when the *p*-value is greater than 0.05, the item of the model is not significant [36]. In Table 9, a p-value < 0.01 is found in the prediction models of *MT* and *SEA*, which indicates that the prediction models have high good fitting and statistical significance and that the predicted values well fit with the experimental values. Lack of fit (LOF) is also used to evaluate the reliability of the prediction model [37]. The p-values of the LOF of the prediction models are 0.6582 and 0.2854, respectively, which indicates that the prediction models have no significant relative pure error and that the experimental values can be described by the prediction models.

Table 9. ANOVA results for the complete quadratic model of *MT* and *SEA*.

Source	Degree of Freedom	Model of *MT*				Model of *SEA*			
		Sum of Squares	Mean Square	F-Value	p-Value	Sum of Squares	Mean Square	F-Value	p-Value
Model	9	828.78	92.09	26.29	8.30×10^{-6} **	9.20×10^{9}	1.02×10^{9}	37.95	1.46×10^{-6} **
A	1	331.38	331.38	94.62	2.05×10^{-6} **	5.98×10^{9}	5.98×10^{9}	222.11	3.72×10^{-8} **
B	1	72.66	72.66	20.75	1.05×10^{-3} **	5.01×10^{8}	5.01×10^{8}	18.61	1.53×10^{-3} **
C	1	220.40	220.40	62.93	1.27×10^{-5} **	2.26×10^{9}	2.26×10^{9}	83.84	3.54×10^{-6} **
A^2	1	190.62	192.86	55.07	2.26×10^{-5} **	3.01×10^{8}	2.90×10^{8}	10.77	8.27×10^{-3} **
B^2	1	6.31	6.15	1.75	0.21	1.69×10^{6}	1.76×10^{6}	0.07	0.80
C^2	1	0.04	0.04	0.01	0.91	1.20×10^{5}	1.20×10^{5}	0.00	0.95
$A * B$	1	1.12	1.12	0.32	0.58	7.71×10^{7}	7.71×10^{7}	2.86	0.12
$A * C$	1	6.12	6.12	1.75	0.22	7.48×10^{7}	7.48×10^{7}	2.78	0.13
$B * C$	1	0.13	0.13	0.04	0.85	3.60×10^{6}	3.60×10^{6}	0.13	0.72
Residual	10	35.02	3.50			2.69×10^{8}	2.69×10^{7}		
Lack of fit	5	14.19	2.84	0.68	0.66	1.70×10^{8}	3.40×10^{7}	1.71	0.29
Pure error	5	20.83	4.17			9.94×10^{7}	1.99×10^{7}		
Total	19	863.80				9.47×10^{9}			

Note: (*) $p < 0.05$, (**) $p < 0.01$.

The F-value and p-value can be used to judge the significance of different factors on the *MT* and *SEA*. Table 9 shows the F-values and the p-values of different factors. From the results of the ANOVA, it is found that the influences of A, B and C on the *MT* are highly significant. In the results of the interaction terms, the influences of AB, AC and BC are not significant. In the results of the compound terms, the influence of A^2 is highly significant, whereas the influences of B^2 and C^2 are not significant. It can be seen from the F-value and p-value of ANOVA that the influences of the factors on the *MT* are shown in order from strong to weak as follows: gas flow rate, slag thickness and liquid depth. For the prediction model of the *SEA*, the influences of A, B and C on the *MT* are highly significant. In the results of the interaction terms, the influences of AB, AC and BC are not significant. In the results of the compound terms, the influence of A^2 is highly significant, whereas the influences of B^2 and C^2 are not significant. It can be seen from the F-value and p-value of ANOVA that the influences of the factors on the *SEA* are shown in order from strong to weak as follows: gas flow rate, slag thickness and liquid depth.

Figure 7 shows the normal probability distributions of the residuals of *MT* and *SEA*. In Figure 7, the residual scatters of the models are roughly distributed on a straight line, which indicates that the errors are normally distributed and the models fit well [38]. Figure 8 shows the comparison between actual and predicted values of *MT* and *SEA*. In Figure 8, the scatters of the actual values and the predicted values are basically distributed on a straight line, which indicates that the prediction models have a high degree of fit. To sum up, the prediction models of *MT* and *SEA* based on RSM are reliable.

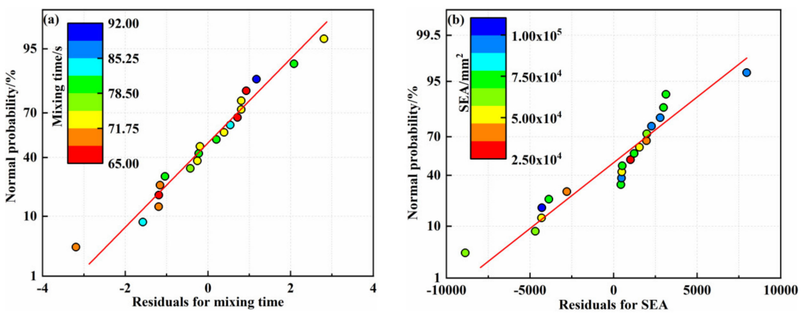

Figure 7. Normal probability distributions of residuals for (**a**) *MT* and (**b**) *SEA*.

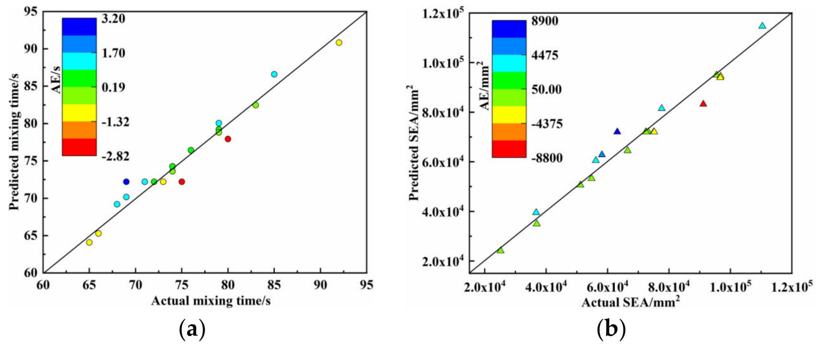

Figure 8. Comparison between actual and predicted values for (**a**) *MT* and (**b**) *SEA*.

4.2.3. Visual Analysis of Response Surface

1. Interactive effects of different factors on *MT*

Under different factors, the RSM was used to carry out quadratic multiple regression analysis on the *MT*, and the 3D response surface diagrams of *MT* were obtained at different factor levels, as shown in Figure 9. The interaction effects of gas flow rate, liquid depth and slag thickness on the *MT* can be observed more intuitively by using the 3D response surface diagram. The larger slope of the response surface is a factor, the more significant the factor effects on the *MT* [34].

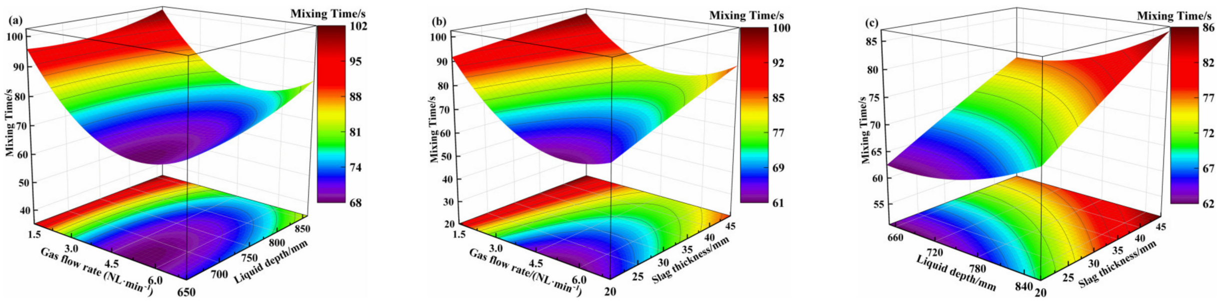

Figure 9. The 3D response surface diagram of *MT* under the interaction of (**a**) gas flow rate and liquid depth, (**b**) gas flow rate and slag depth, (**c**) liquid depth and slag depth.

Figure 9a shows the interaction effect of gas flow rate and liquid depth on the *MT* at a slag thickness of 32.5 mm. The *MT* first decreases and then increases with the increase in gas flow rate. With the increase in liquid depth, the *MT* also increases. Compared with the response surface in the direction of liquid depth, the slope of the response surface in the direction of gas flow rate is larger and the contour density in the direction of gas flow rate is higher than that in the direction of liquid depth, which indicates that the effect of gas flow rate on *MT* is larger than that in the direction of liquid depth. Moreover, this result is confirmed by the smaller p-value of gas flow rate than that of liquid depth in Table 9.

Figure 9b shows the interaction effect of gas flow rate and slag thickness on the *MT* at a liquid depth of 760.5 mm. Similarly to the effect of liquid depth on *MT*, the *MT* increases with the increase in slag thickness. It can be seen that the gas flow rate has a more significant influence on the *MT* than the slag thickness by comparing the slope and the contour density of the response surface.

Figure 9c shows the interaction effect of liquid depth and slag thickness on the *MT* at a gas flow rate of 4.3 NL·min^{-1}. It can be seen that the slag thickness has a more significant influence on the *MT* than the liquid depth by comparing the slope and the contour density of the response surface. To sum up, the different impacts of factors on *MT* are shown in order from strong to weak as follows: gas flow rate, slag thickness and liquid depth, which is consistent with the results of ANOVA in Table 9.

2. Interactive effects of different factors on *SEA*

Figure 10 shows the 3D response surface diagrams of *SEA* under different factor levels. Figure 10a shows the interaction effect of gas flow rate and liquid depth on the *SEA* at a slag thickness of 32.5 mm. The *SEA* increases with the increase in gas flow rate and liquid depth. Meanwhile, the gas flow rate has a more significant influence on the *SEA* than the liquid depth by comparing the slope and the contour density of the response surface.

Figure 10b shows the interaction effect of gas flow rate and slag thickness on the *SEA* at a liquid depth of 760.5 mm. The *SEA* decreases with the increase in slag thickness. Moreover, the slag thickness has a greater influence on the *SEA* under the condition of high gas flow rate than \under the condition of low gas flow rate by comparing the slope and the contour density of the response surface.

Figure 10c shows the interaction effect of liquid depth and slag thickness on the *SEA* at a gas flow rate of 4.3 NL·min^{-1}. It can be seen that the slag thickness has a more significant influence on the *SEA* than the liquid depth by comparing the slope and the contour density of the response surface. To sum up, the different impacts of factors on *SEA* are shown in order from strong to weak as follows: gas flow rate, slag thickness and liquid depth, which is consistent with the results of ANOVA in Table 9.

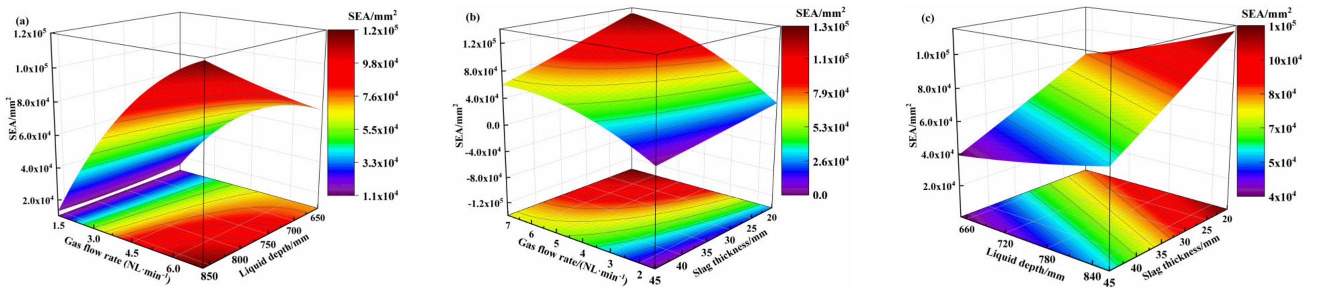

Figure 10. The 3D response surface diagram of *SEA* under the interaction of (**a**) gas flow rate and liquid depth, (**b**) gas flow rate and slag depth, (**c**) liquid depth and slag depth.

4.2.4. Multiobjective Optimization and Experimental Verification

To achieve the production goal of high-efficiency refining and high cleanliness molten steel in industrial production, the argon bottom blowing of LF should meet the requirements of short *MT* and small *SEA*. Therefore, the optimization goals were set to the minimum responses to obtain the minimum *MT* and *SEA*, and the importance of the two optimization goals was set to 1 using Minitab software. The design variable optimization objectives of gas flow rate and slag thickness were set as "range constraint", and the liquid depth was set as "retention value". The optimization constraints are shown in Table 10.

Table 10. Optimization constraints.

Parameter	Goal	Range	Importance
Gas flow rate (NL·min^{-1})	Range constraint	1.95–6.6	-
Liquid depth/mm	Retention value	760.5, 814, 850	-
Slag thickness/mm	Range constraint	21.6–43.4	-
MT/s	Range constraint	65–92	1
SEA/mm^2	Range constraint	25,140.8–110,356	1

The final optimal parameters are as follows: (1) Gas flow rate of 3.8 NL·min^{-1}, liquid depth of 760.5 mm, slag thickness of 35.5 mm and under the optimized conditions, the *MT* and the *SEA* calculated by prediction models are 76 s and 59,070 mm^2, respectively. (2) Gas flow rate of 3.4 NL·min^{-1}, liquid depth of 814 mm, slag thickness of 30 mm and under the optimized conditions, the *MT* and the *SEA* calculated by prediction models are 78 s and 65,770 mm^2, respectively. (3) Gas flow rate of 3.2 NL·min^{-1}, liquid depth of 850 mm, slag thickness of 26.2 mm and under the optimized conditions, the *MT* and the *SEA* calculated by prediction models are 80 s and 71,516 mm^2, respectively. Meanwhile, the model verification experiment was carried out under the optimal parameters as shown in Table 11. In Table 11, it can be seen that the *MT* and the *SEA* of different conditions are 75 s and 57,830 mm^2, 79 s and 62,996 mm^2, 82 s and 73,938 mm^2, respectively. Moreover, compared with the predicted values, the errors of *MT* and the *SEA* of different conditions from the experimental values are 1.3% and 2.1%, 1.3% and 4.2%, 2.5% and 3.4%, respectively. The results show that the prediction models of *MT* and *SEA* established in this study are reliable, which further verifies that the multiobjective collaborative optimization of argon bottom blowing of LF using RSM is feasible. Meanwhile, the modeling method and workflow in this study can also be applied in the research of argon bottom blowing of LF based on numerical simulation to reduce the simulation times and improve the simulation efficiency.

Table 11. Predicted and experimental values under optimal conditions.

Number	Gas Flow Rate (NL·min^{-1})	Liquid Depth/mm	Slag Thickness/mm	*MT*/s (Predicted Value)	*MT*/s (Experimental Value)				Error/%
					1st	2nd	3rd	AVG	
1	3.8	760.5	35.5	76	77	74	75	75	1.3
2	3.4	814	30	78	76	83	79	79	1.3
3	3.2	850	26.2	80	86	76	85	82	2.5

Number	Gas Flow Rate (NL·min^{-1})	Liquid Depth/mm	Slag Thickness/mm	*SEA*/mm^2 (Predicted Value)	*SEA*/mm^2 (Experimental Value)						Error/%
					1st	2nd	3rd	4th	5th	AVG	
1	3.8	760.5	35.5	59,070	63,146	55,115	56,581	56,366	57,940	57,830	2.1
2	3.4	814	30	65,770	64,544	65,648	62,149	63,415	59,226	62,996	4.2
3	3.2	850	26.2	71,516	73,491	80,491	71,421	69,444	74,846	73,939	3.4

Note: 1st, 2nd, 3rd, 4th, 5th and AVG represent the first experimental value, the second experimental value, the third experimental value, the fourth experimental value, the fifth experimental value and the average experimental value, respectively.

5. Conclusions

In this study, the effects of gas flow rate, molten steel depth and slag thickness on *MT* and the *SEA* were studied by single factor analysis. Meanwhile, the prediction models of *MT* and the *SEA* were established based on RSM and multiobjective collaborative optimization and the following conclusions can be drawn:

(1) The hydraulic experiment shows that when the identical porous plug radial position is 0.6R and the separation angle is 135°, the mixing efficiency is the best and this arrangement of porous plugs can avoid serious scour to the lining of the ladle. With the increase in the gas flow rate, the *MT* first decreases and then increases and the *SEA* increases. With the increase in the liquid depth, the *MT* and the *SEA* increase. With the increase in slag thickness, the *MT* increases and the *SEA* decreases;

(2) The p-values of response surface models designed based on the CCD principle of *MT* and *SEA* are all less than 0.01, and the values of Adj-R^2 are 0.923 and 0.946, respectively, which indicate that these models fit well and have statistical significance. Meanwhile, it can be seen from the F-value and p-value of ANOVA that the different impacts of factors on *MT* are shown in order from strong to weak as follows: gas flow rate, slag thickness, liquid depth; the different impacts of factors on *SEA* are shown in order from strong to weak as follows: gas flow rate, slag thickness, liquid depth;

(3) The optimal gas flow rate, slag thickness and the corresponding *MT* and *SEA* were obtained under the three liquid depths when the *MT* and *SEA* were set as a minimum. Meanwhile, the model verification experiment was carried out under the optimal parameters. The results show that the experimental values are in good agreement with the predicted values, which further verifies that the multiobjective collaborative optimization of argon bottom blowing in LF using RSM is feasible.

Author Contributions: Conceptualization, Z.X.; methodology, Z.X.; validation, J.S. and B.H.; data curation, J.Z. (Junguo Zhang); writing—original draft preparation, Z.X.; writing—review and editing,

J.Z. (Jiangshan Zhang) and Q.L.; supervision, J.Z. (Jiangshan Zhang) and Q.L. All authors have read and agreed to the published version of the manuscript.

Funding: This research was funded by the National Natural Science Foundation of China (No. 51974023), and the funding of State Key Laboratory of Advanced Metallurgy, University of Science and Technology Beijing (No. 41621005).

Institutional Review Board Statement: Not applicable.

Informed Consent Statement: Not applicable.

Data Availability Statement: Not applicable.

Conflicts of Interest: The authors declare no conflict of interest.

References

1. Dong, P.-L. Physical modeling for optimization of bottom blowing argon process in a 210t ladle. *Iron Steel* **2016**, *51*, 41–44. [CrossRef]
2. Xin, Z.-C.; Zhang, J.-S.; Jin, Y.; Zheng, J.; Liu, Q. Predicting alloying element yield in a ladle furnace using PCA-DNN model. *Int. J. Miner. Metall. Mater.* **2021**. [CrossRef]
3. Liu, Z.-Q.; Li, L.-M.; Li, B.-K. Modeling of gas-steel-slag three-phase flow in ladle metallurgy: Part I. Physical modeling. *ISIJ Int.* **2017**, *57*, 1971–1979. [CrossRef]
4. Han, J.-J.; Li, S.-Q.; Wu, L. Stirring characteristics of argon blowing from the ladle bottom. *J. Univ. Sci. Technol. Beijing* **2011**, *33*, 1085–1090. [CrossRef]
5. Li, J.-P.; Liu, Y.; Cheng, S.-S. Research of bottom blowing and slag layer thickness on bath stirring in a 120t ladle. In Proceedings of the 2nd International Conference on Advanced Materials and Intelligent Manufacturing, Nanning, China, 20–22 August 2021.
6. Villela-Aguilar, J.-D.-J.; Ramos-Banderas, J.-A.; Hernández-Bocanegra, C.-A.; Uriostegui-Hernandez, A.; Solorio-Diaz, G. Optimization of the mixing time using asymmetrical arrays in both gas flow and injection positions in a dual-plug ladle. *ISIJ Int.* **2020**, *60*, 1172–1178. [CrossRef]
7. Liu, H.-P.; Qi, Z.-Y.; Xu, M.-G. Numerical simulation of fluid flow and interfacial behavior in three-phase argon-stirred ladles with one plug and dual plugs. *Steel Res. Int.* **2011**, *82*, 440–458. [CrossRef]
8. Herrera-Ortega, M.; Ramos-Banderas, J.-A.; Hernandez-Bocanegra, C.-A.; Montes-Rodríguez, J.-J. Effect of the location of tracer addition in a ladle on the mixing time through physical and numerical modeling. *ISIJ Int.* **2021**, *61*, 2185–2192. [CrossRef]
9. Mandal, J.; Patil, S.; Madan, M.; Mazumdar, D. Mixing time and correlation for ladles stirred with dual porous plugs. *Metall. Mater. Trans. B* **2005**, *36*, 479–487. [CrossRef]
10. Zhu, M.-Y.; Inomoto, T.; Sawada, I.; Hsiao, T.-C. Fluid flow and mixing phenomena in the ladle stirred by argon through multi-tuyere. *ISIJ Int.* **1995**, *35*, 472–479. [CrossRef]
11. Morales, R.-D.; Calderon-Hurtado, F.-A.; Chattopadhyay, K. Demystifying underlying fluid mechanics of gas stirred ladle systems with top slag layer using physical modeling and mathematical modeling. *ISIJ Int.* **2019**, *59*, 1224–1233. [CrossRef]
12. Liu, W.; Tang, H.-Y.; Yang, S.-F.; Wang, M.-H.; Li, J.-S.; Liu, Q.; Liu, J.-H. Numerical simulation of slag eye formation and slag entrapment in a bottom-blown argon-stirred ladle. *Metall. Mater. Trans. B* **2018**, *49*, 2681–2691. [CrossRef]
13. Peranandhanthan, M.; Mazumdar, D. Modeling of slag eye area in argon stirred ladles. *ISIJ Int.* **2010**, *50*, 1622–1631. [CrossRef]
14. Li, L.-M.; Li, B.-K.; Liu, Z.-Q. Modeling of gas-steel-slag three-phase flow in ladle metallurgy: Part II. Multi-scale mathematical model. *ISIJ Int.* **2017**, *57*, 1980–1989. [CrossRef]
15. Li, Q.; Pistorius, P.-C. Interface-resolved simulation of bubbles-metal-slag multiphase system in a gas-stirred ladle. *Metall. Mater. Trans. B* **2021**, *52*, 1532–1549. [CrossRef]
16. Conejo, A.-N.; Mishra, R.; Mazumdar, D. Effects of nozzle radial position, separation angle, and gas flow partitioning on the mixing, eye area, and wall shear stress in ladles fitted with dual plugs. *Metall. Mater. Trans. B* **2019**, *50*, 1490–1502. [CrossRef]
17. Conejo, A.-N.; Feng, W.-H. Ladle eye formation due to bottom gas injection: A reassessment of experimental data. *Metall. Mater. Trans. B* **2022**, *53*, 999–1017. [CrossRef]
18. Krishnapisharody, K.; Irons, G.-A. Modeling of slag eye formation over a metal bath due to gas bubbling. *Metall. Mater. Trans. B* **2006**, *37*, 763–772. [CrossRef]
19. Leung, M.-F.; Wang, J. A collaborative neurodynamic approach to multiobjective optimization. *IEEE Trans. Neural Netw. Learn. Syst.* **2018**, *29*, 5738–5748. [CrossRef]
20. Wang, Z.-K.; Zhen, H.-L.; Deng, J.-D.; Zhang, Q.-F.; Li, X.-J.; Yuan, M.-X.; Zeng, J. Multiobjective optimization-aided decision-making system for large-scale manufacturing planning. *IEEE Trans. Cybern.* **2021**. [CrossRef]
21. Nole, M.-L.; Soler, D.; Higuera-Trujillo, J.-L.; Llinares, C. Optimization of the cognitive pro-cesses in a virtual classroom: A multi-objective integer linear programming approach. *Mathematics* **2022**, *10*, 1184. [CrossRef]
22. Zhou, G.-S.; Ma, J.-Y.; Tang, Y.-P.; Wang, X.-M.; Zhang, J.; Yao, X.; Jiang, W.; Duan, J.-A. Optimization of ultrasound-assisted extraction followed by macroporous resin purification for maximal recovery of functional components and removal of toxic components from ginkgo biloba leaves. *BioMed Res. Int.* **2018**, *2018*, 4598067. [CrossRef]

23. Yang, Z.-J.; Wang, K.-K.; Yang, Y. Optimization of ECAP-RAP process for preparing semisolid billet of 6061 aluminum alloy. *Int. J. Miner. Metall. Mater.* **2020**, *27*, 792–800. [CrossRef]
24. Eskandari, B.; Bhowmick, S.; Alpas, A.-T. Turning of Inconel 718 using liquid nitrogen: Multi-objective optimization of cutting parameters using RSM. *Int. J. Adv. Manuf. Technol.* **2022**, *120*, 3077–3101. [CrossRef]
25. Sivalingam, V.; Zhao, Y.-Z.; Thulasiram, R.; Sun, J.; Guo, K.; Nagamalai, T. Machining behaviour, surface integrity and tool wear analysis in environment friendly turning of Inconel 718 alloy. *Measurement* **2021**, *174*, 109028. [CrossRef]
26. Hu, Q.; Li, X.-S.; Zhang, J.-Q.; Lian, Y.-X.; Tang, H.-Y. Effect of differential flowrate argon blowing mode on mixing and top slag behavior for a 150 t ladle. *Iron Steel* **2020**, *55*, 31–38. [CrossRef]
27. Zheng, S.-G.; Zhu, M.-Y. Water model study on removing inclusions in a ladle with argon injected through nozzle and porous plug. *ACTA Metall. Sin.* **2006**, *42*, 1143–1148.
28. Cao, L.-L.; Liu, Q.; Wang, Y.-N.; Lin, W.-H.; Sun, J.-K.; Sun, L.-F.; Guo, W.-D. An Attempt to visualize the scrap behavior in the converter for steel manufacturing process using physical and mathematical methods. *Mater. Trans.* **2018**, *59*, 1829–1836. [CrossRef]
29. Cao, L.-L.; Wang, Y.-N.; Liu, Q.; Feng, X.-M. Physical and mathematical modeling of multiphase flows in a converter. *ISIJ Int.* **2018**, *58*, 573–584. [CrossRef]
30. Sun, J.-K.; Zhang, J.-S.; Lin, W.-H.; Feng, X.-M.; Liu, Q. Effect of bottom blowing mode on fluid flow and mixing behavior in converter. *Metals* **2022**, *12*, 117. [CrossRef]
31. Zheng, W.; Tu, H.; Li, G.-Q.; Shen, X.; Xu, Y.-L.; Zhu, C.-Y.; Lu, K. Physical simulation of refining process optimization for bottom argon blowing in a 250 t ladle. *J. Univ. Sci. Technol. Beijing* **2014**, *36*, 53–59. [CrossRef]
32. Jonsson, L.; Jonsson, P. Modeling of fluid flow conditions around the slag/metal interface in a gas-stirred ladle. *ISIJ Int.* **1996**, *36*, 1127–1134. [CrossRef]
33. Mondal, M.; Ghosh, A.; Gayen, K.; Halder, G.; Tiwari, O.-N. Carbon dioxide bio-fixation by *Chlorella* sp. BTA 9031 towards biomass and lipid production: Optimization using central composite design approach. *J. CO_2 Util.* **2017**, *22*, 317–329. [CrossRef]
34. Bao, J.-W.; Liu, Z.-G.; Chu, M.-S.; Han, D.; Cao, L.-G.; Guo, J.; Zhao, Z.-C. Multi-objective collaborative optimization of metallurgical properties of iron carbon agglomerates using response surface methodology. *Int. J. Miner. Metall. Mater.* **2021**, *28*, 1917–1928. [CrossRef]
35. Xiao, Z.-Q.; Peng, Y.-C. Mathematical modelling of entrapment phenomena at slag/metal interface in gas-stirred ladle. *Iron Steel* **1989**, *24*, 17–21. [CrossRef]
36. Xin, Z.-C.; Zhang, J.-S.; Lin, W.-H.; Zhang, J.-G.; Jin, Y.; Zheng, J.; Cui, J.-F.; Liu, Q. Sulphide capacity prediction of CaO-SiO_2-MgO-Al_2O_3 slag system by using regularized extreme learning machine. *Ironmak. Steelmak.* **2020**, *48*, 275–283. [CrossRef]
37. Zhang, L.-J.; Zhou, H.-B. Recovery of Cu from waste copper clad laminate sorting residue in a two-stage bioleaching process: Process optimization and mechanisms. *Chin. J. Eng.* **2022**. [CrossRef]
38. Zhang, X.-R.; Liu, Z.-H.; Fan, X.; Lian, X.; Tao, C.-Y. Optimization of reaction conditions for the electroleaching of manganese from low-grade pyrolusite. *Int. J. Miner. Metall. Mater.* **2015**, *22*, 1121–1130. [CrossRef]